Letter

Lattice-driven chiral charge density wave state in 1*T*-TaS_2

Manoj Singh,[1] Boning Yu,[1] James Huber,[1] Bishnu Sharma,[1] Ghilles Ainouche,[1] Ling Fu,[1] Jasper van Wezel,[2] and Michael C. Boyer[1,*]

[1]*Department of Physics, Clark University, Worcester, Massachusetts 01610, USA*

[2]*Institute for Theoretical Physics Amsterdam, University of Amsterdam, Science Park 904,1098 XH Amsterdam, The Netherlands*

(Received 7 December 2021; revised 27 July 2022; accepted 2 August 2022; published 19 August 2022)

We use scanning tunneling microscopy to study the domain structure of the nearly commensurate charge density wave (NC-CDW) state of 1*T*-TaS_2. In our subangstrom characterization of the state, we find a continual evolution of the CDW lattice from domain wall to domain center, instead of a fixed CDW arrangement within a domain. Further, we uncover an intradomain chirality characterizing the NC-CDW state. Unlike the orbital-driven chirality previously observed in related transition-metal dichalcogenides, the chiral nature of the NC-CDW state in 1*T*-TaS_2 appears driven by a strong coupling of the NC-CDW state to the lattice.

DOI: 10.1103/PhysRevB.106.L081407

The complexity of the physics driven by electron-electron and electron-phonon interactions makes the transition-metal dichalcogenides (TMDs) a fertile playground to study complex orders as well as their coexistence with and evolution to other quantum orders. 1*T*-TaS_2 has been cited as a "protypical" TMD compound [1,2] in which to explore such interplay, though it also hosts some unique physics among the TMDs resulting in intense interest in this particular compound. Initially, the correlated metallic TMD received attention for its four distinct charge density wave (CDW) phases [3–5]. 1*T*-TaS_2 has also garnered extensive interest for a potential low-temperature Mott insulating state, not found in the other TMDs, coexisting with the low-temperature CDW state [6–10] drawing comparisons to high-temperature superconducting and heavy fermion systems [11].

The proximity of multiple quantum orders in 1*T*-TaS_2 has led to an interest in tuning these electron-electron and electron-phonon interactions to alter and control the material's electronic and structural properties. Elemental doping has led to the emergence of superconductivity [12,13] and to the reported evolution of the Mott insulating state to a metallic state [14]. Perturbations induced by electromagnetic fields and strain have led to new stable electronic states [8,15–18]. The application of pressure has led to the emergence of superconductivity and coexistence of the superconducting state with a CDW state [19,20]. Altering the thickness of 1*T*-TaS_2 crystals provides another mechanism by which to control the 1*T*-TaS_2 phase diagram [21,22]. The diverse ways in which 1*T*-TaS_2 can be tuned leads to rich phase diagrams reminiscent of those seen for high-temperature superconducting and heavy fermion systems [23]. Emerging from these studies is a better understanding not only of the fundamental physics hosted by the 1*T*-TaS_2 but also of the mechanisms by which to appropriately tailor the material's properties for possible future applications in electronics and data storage. Very recently, the previously reported achiral 1*T*-TaS_2 has induced-chiral CDW domains with Ti doping [24], opening additional paths for electronic applications through the possibility of chiral domain switching [25].

Here, we focus on our scanning tunneling microscopy (STM) studies of the nearly commensurate CDW (NC-CDW) state of 1*T*-TaS_2. Figure 1(a) shows the crystal structure for the undistorted material. At a temperature of ∼543 K, the Ta ions in the S-Ta-S layers distort and 1*T*-TaS_2 transitions from a metallic to an incommensurate CDW (I-CDW) state [5]. At temperatures below ∼180 K, 1*T*-TaS_2 enters a commensurate CDW (C-CDW) state. In this CDW state, 12 Ta ions distort toward a central Ta ion in a star-of-David-like pattern [26]. These stars then create a $\sqrt{13}a_0 \times \sqrt{13}a_0$ commensurate pattern across the layer.

Between the I-CDW and C-CDW phases resides the NC-CDW state. The transition from the IC-CDW to the NC-CDW state occurs at ∼350 K [29]. The NC-CDW state is commonly characterized as having hexagonally ordered C-CDW domains separated by an IC-CDW domain-wall network or by discommensurations [8,22,30,31]. However, as has previously been noted [5], this description may be a simplification of the true NC-CDW domain structure. Lacking is a characterization of the NC-CDW state which details with subangstrom resolution the evolution of the CDW state from the domain wall to the domain center. Given that distortions of Ta ions within 1*T*-TaS_2 are fundamental to driving the observed CDW states and electronic properties of the material, there is an essential need to better characterize and understand the nanoscale modulations of the NC-CDW state. Furthermore, as we characterize the NC state in 1*T*-TaS_2, we uncover an intradomain CDW chirality which, to the best of our knowledge, has not been reported previously.

Figure 1(b) shows an STM topographic image of the NC-CDW state we acquired at room temperature. The acquired image shows a roughly hexagonally ordered domain pattern characteristic of the NC state. The fast Fourier transform (FFT) of the image [Fig. 1(c)] evinces essential peaks from

*Author to whom correspondence should be addressed: mboyer@clarku.edu

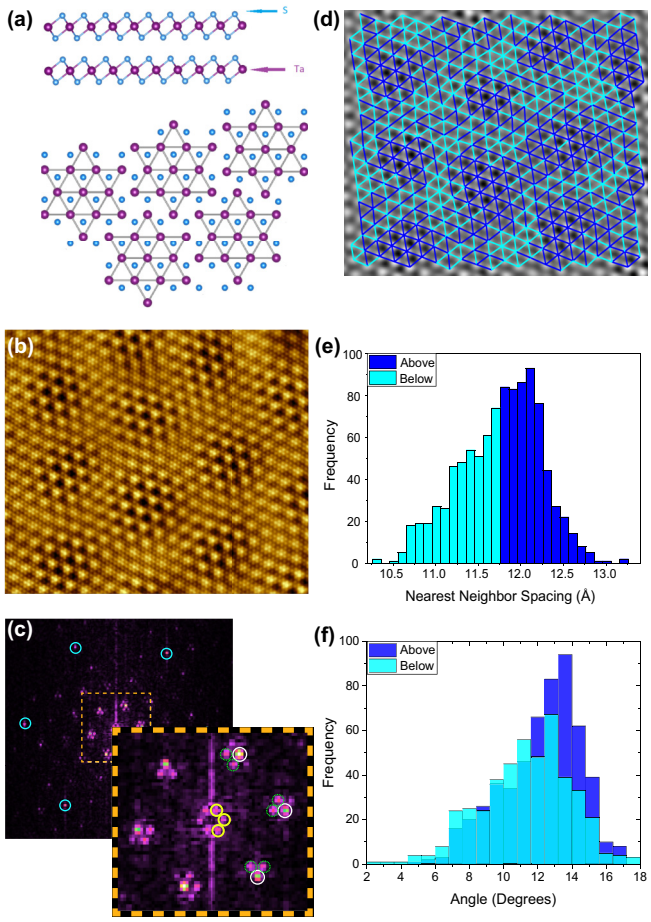

FIG. 1. (a) Top: Layered crystal structure for $1T$-TaS_2. Bottom: Top view showing Ta-formed stars of David. Surface S ions, directly imaged by STM, are superimposed for reference. Crystal structure created using VESTA [27]. (b) 230 Å × 200 Å STM topography (I = 450 pA and $V_{\mathrm{Bias}} = 150$ mV). Image was Fourier filtered to include signals identified in (c). Zoom of single domain in Supplemental Material [28]. (c) Fourier transform of 230 Å × 200 Å topographic image at left. Atomic signals are circled in blue. The large orange dotted square is a zoom of the central FFT region. Within this central region are low wave-vector peaks (yellow) and average CDW peaks (white) around which there are satellite peaks (dotted green). (d) Connections between NN CDW maxima superimposed on a Fourier filtered topographic image (now grayscale). The filtered image shows only locations of CDW maxima. The average NN distance is 11.76 Å. Blue (cyan) connections show NN separations above (below) 11.76 Å threshold. (e) Histogram of NN distances with 0.1 Å bin size, reflecting image resolution. (f) Angles of NN connectors relative to the atomic lattice. Blue (cyan) shows angular distributions for connectors above (below) 11.76 Å threshold.

which we extract average quantities characterizing the NC-CDW state. We find the CDW superlattice to have an average periodicity of 11.76 Å at an average angle of 11.8° relative to the atomic lattice, in agreement with previous STM, x-ray, and electron diffraction measurements [3,5,26]. Using the position of satellite peaks relative to the CDW peaks allows us to determine the average domain periodicity of 73 Å, also in agreement [5,32].

To fully understand the NC-CDW state requires going beyond average quantities. To do this, we focus only on the CDW superlattice and Fourier filter our topographic image such that only the central CDW and surrounding satellite peaks are included [Fig. 1(d)]. We next calculate the nearest-neighbor (NN) distances between CDW maxima so as to understand the distribution of distances. We find a large range of NN distances spanning 10.26–13.22 Å. Superimposed on the image in Fig. 1(d) are line segments connecting the CDW maxima which are color coded according to the 11.76 Å threshold with segments colored dark blue (cyan) being greater (smaller) than the threshold. Generally, the CDW maxima have a greater spacing within the domain than in the domain walls.

In the NC-CDW state, the CDW lattice is rotated relative to the atomic lattice. This is seen in Fig. 1(c) where the CDW peaks are rotated by 11.8° relative to the atomic peaks in the FFT, in agreement with angles as measured by electron-diffraction [20] and STM measurements [3] acquired at this temperature. Using the NN distance threshold of 11.76 Å, we create histograms for the local CDW lattice rotation relative to the atomic lattice for NNs above and below the threshold as seen in Figs. 1(e) and 1(f). While the average relative angle for NN above the distance threshold (those generally within a domain) of 12.1° is greater than the average for those below (those generally within the domain wall) of 11.3°, there is a wide range of angles within each grouping.

To obtain a better idea of the evolution of the CDW spacing and angles from domain wall to domain center, we employ a local masking technique. For a given domain, we identify all CDW maxima with an intensity which is within 95% of the maximum CDW intensity as the domain center. We then calculate the NN distances among each of these CDW peaks, thereby quantifying NN distances at the center of the domain [Fig. 2(a), blue]. We next include the NN CDW peaks to the domain center CDW peaks and recalculate NN distances omitting the NN domain center values [Fig. 2(a), red]. We then include the next-nearest-neighbor (NNN) peaks [Fig. 2(a), green]. Finally, we include all remaining CDW peaks [Fig. 2(a), cyan] allowing us to determine the evolution of the NN distances progressing from domain walls to domain centers [Fig. 2(b)]. Obvious from the histograms are (1) an increase in NN spacing and (2) a narrowing of the distribution width as one moves from the domain walls toward the domain center. These two apparent progressions are confirmed with the evolution of the mean and standard deviation of 11.54 ± 0.52 Å (cyan) to 11.75 ± 0.49 Å (green) to 12.06 ± 0.27 Å (red) to 12.14 ± 0.20 Å (blue). We note that the NN spacing in our measurements directly at the domain center is slightly larger than the fixed NN CDW spacing of the low-temperature C-CDW state. Using the same groupings, we determine the local CDW lattice angle relative to the atomic lattice. There is a similar evolution in the mean and distribution width of the CDW angle toward the low-temperature commensurate value of 13.9° as one progresses from the domain walls to the domain centers [Fig. 2(c)]: 10.1° ± 2.5° (cyan) to 11.9° ± 2.4° (green) to 13.4° ± 1.2°(red) to 13.7° ± 0.9° (blue).

Underlying crystal disorder and defects within a sample can obscure fundamental/overarching characteristics within a material. To obtain a clearer progression of the NN distances

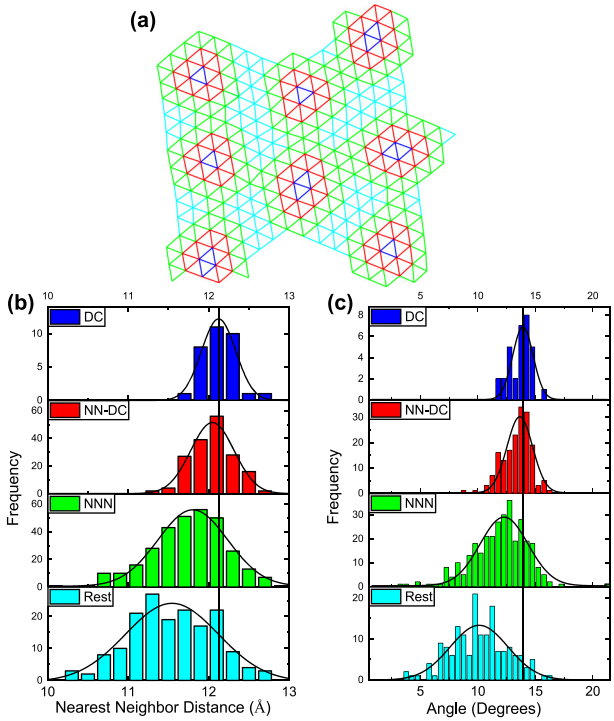

FIG. 2. (a) Domain center (blue) found using local intensity thresholding. NN-DC (red): Nearest-neighbor CDW connectors towards the domain center (excludes blue connectors). NNN (green): Next-nearest-neighbor connectors towards domain center (excludes blue and red). Rest (cyan): The remaining connectors (excludes blue, red, green). Domains with centers near the edge of the topography are ignored. (b) Histograms of NN distances for each connector grouping with 0.2 Å bin size. (c) Histograms of CDW angles relative to the atomic lattice for each connector grouping. Gaussian fits and the vertical line at the DC peak are superimposed in (b) and (c) to illustrate the evolution of the peak location and width.

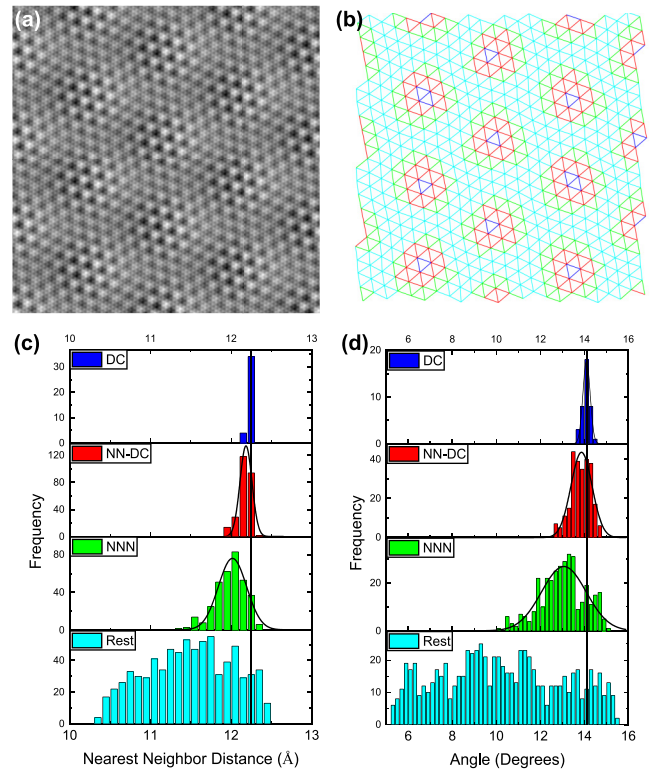

FIG. 3. (a) 253 Å × 253 Å computer-simulated STM topography. Average intensity and wave vectors for atomic, CDW, satellite, and low-wave-vector peaks from Fig. 1(c) were used to create image (see Supplemental Material [28]). (b) From intensity thresholding: Domain center (blue). NN-DC (red): Nearest-neighbor CDW connectors towards the domain center (excludes blue connectors). NNN (green): Next-nearest-neighbor connectors towards the domain center (excludes blue and red). Rest (cyan): Remaining connectors (excludes blue, red, green). (c) Histograms of NN distances for each connector grouping. Statistics: 11.48 ± 0.53 Å (cyan) to 11.98 ± 0.19 Å (green) to 12.16 ± 0.08 Å (red) to 12.23 ± 0.03 Å (blue). (d) Histograms of CDW angles relative to the atomic lattice for each connector grouping. Statistics: $10.2^\circ \pm 2.7^\circ$ (cyan) to $13.0^\circ \pm 1.0^\circ$ (green) to $13.8^\circ \pm 0.5^\circ$ (red) to $14.1^\circ \pm 0.2^\circ$ (blue). Gaussian fits and the vertical line at the DC peak are superimposed in (c) and (d) to illustrate the evolution of the peak location and width.

from the domain walls to the domain center, we used the wave vectors extracted from the FFT [Fig. 1(c)] to simulate our topographic image [Fig. 3(a)]. Our simulated topography well matches our topographic image in Fig. 1(b). Using intensity thresholding we calculate NN distances and angles starting at the domain centers and progressing toward the domain walls [Fig. 3(b)]. The histograms appearing in Figs. 3(c) and 3(d) illustrate the range of values and confirm the progression found in the data: The average NN CDW spacing and angle continually increase from domain wall to domain center, and the width of the distributions narrows only approaching values found for the low-temperature C-CDW state near the center of a domain.

Having elucidated the spacing and local angle of the CDW evolution from domain wall to domain center, we study the connection satellite peaks [Fig. 1(c)] have to the domain structure observed in topographic images. Fourier filtering of the STM-acquired topographic image [Fig. 1(b)] where only the central CDW peaks in the FFT are included [white circles in Fig. 1(c)] produces a topography with a regular hexagonal CDW lattice with NN CDW spacing (and angle relative to the lattice) equal to the average CDW periodicity (and angle) for the material, and which is purely incommensurate with the atomic lattice. We will call this lattice $\mathrm{CDW}_{\mathrm{ave}}$. Including the satellite peaks (in addition to the central CDW peak when Fourier filtering the STM-acquired image) leads to the full NC-CDW lattice with domain structure as seen in Fig. 1(d). We will call this lattice $\mathrm{CDW}_{\mathrm{ltc}}$. We now compare the two images. Figure 4(a) shows the locations for CDW maxima for (1) $\mathrm{CDW}_{\mathrm{ave}}$ (black dots) and (2) $\mathrm{CDW}_{\mathrm{ltc}}$ (blue dots). Arrows superimposed on this image point from $\mathrm{CDW}_{\mathrm{ave}}$ maxima to the nearest $\mathrm{CDW}_{\mathrm{ltc}}$ maxima locations, with the length of the arrow proportional to the shift distance.

The shift of the $\mathrm{CDW}_{\mathrm{ltc}}$ maxima locations relative to the $\mathrm{CDW}_{\mathrm{ave}}$ locations varies spatially in a way that mimics the domain pattern of the NC-CDW state. Further, the shift arrows can be used to easily identify the locations and extent of individual domains. Within a domain, each shift arrow has a continual evolution in direction (counterclockwise rotation)

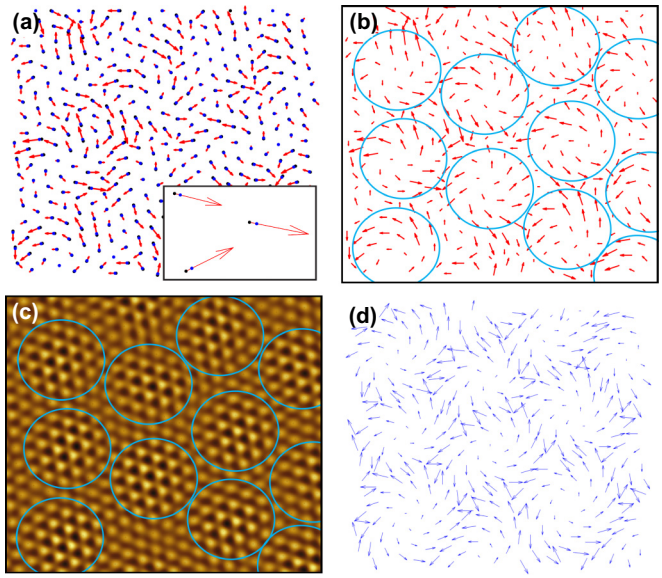

FIG. 4. (a) Arrows point from CDW_{ave} maxima to nearest CDW_{ltc} maxima. The arrow length is proportional to displacement. The inset shows a zoom and illustrates arrows pointing from CDW_{ave} maximum (black) to CDW_{ltc} maximum (blue). (b) Blue circles are superimposed on arrows from (a) as a guide to the eye to show the vortexlike chiral displacement patterns. (c) The same blue circles are superimposed on CDW_{ltc} topography and match domain locations. (d) Arrows are drawn from the CDW_{ave} maximum location to the nearest imaged sulfur ion. An identical, though translated, pattern is produced if arrows are drawn from CDW_{ave} maxima locations to the nearest Ta ions (see Supplemental Material [28]). We chose the sulfur ion for this figure since we image those ions directly and obtain the same information. Note, while the Lawler-Fujita algorithm has proven useful in extracting picometer-scale drift and lattice strain fields [33,34], it is not suitable for use in extracting the local displacement fields shown in this figure (see Supplemental Material [28]).

and size (the shift is smallest at the domain center and largest at the domain edge). In short, we uncover an intradomain chirality of the NC-CDW state which, to the best of our knowledge, has not been reported previously. At the domain wall, there is a sudden shift in this evolution with shift arrows from neighboring domains sometimes pointing in direct opposition to one another. This shift is indicative of the CDW discommensuration between domains. Using the shift arrows as reference, we overlay blue circles as a general guide to the eye to illustrate the domain locations, rough size, and arrangement [Fig. 4(b)]. The same circles are superimposed on the CDW_{ltc} filtered image [Fig. 4(c)] verifying the ability to use the shift arrows to appropriately identify domain locations. Quantifying the CDW_{ltc} shift from the CDW_{ave}, we find an average displacement of 0.72 Å with a maximum displacement of 1.70 Å. This maximum displacement is significant and represents a displacement of ∼14% of the CDW_{ave} lattice spacing. Simulating CDW_{ave} and CDW_{ltc} confirms and provides even clearer evidence of this chirality (see Supplemental Material [28]).

The observed shifts highlight an intrinsic chirality to the NC-CDW state: There is a counterclockwise vortexlike displacement of the CDW_{ltc} maxima relative to the CDW_{ave} locations. The signature of this intradomain chirality is embedded in the satellite peaks in the FFT of the topographic image (see Supplemental Material [28]). While Fig. 1(c) shows multiple satellite peaks around several of the CDW peaks in the FFT, each CDW peak (white circles) has two associated high-intensity satellite peaks (green dotted circles). These two intense satellite peaks rotate clockwise around the CDW peaks as one progresses clockwise around the FFT center. FFTs of our topographic images of the NC-CDW state indeed commonly show two intense satellite peaks which rotate around an average CDW peak and is also commonly seen in other published STM studies of the NC-CDW state of $1T$-TaS_2 [5,17].

Finally, we explore the origin of the chiral nature of the CDW state. A chiral CDW state has been observed in $1T$-$TiSe_2$ [35] and recently in the low-temperature state of Ti-doped $1T$-TaS_2 [24]. The chiral nature these states originates from the orbital structure [24,36–38]. The chirality is detected in FFTs of STM topographies through CDW peak intensities which increase/decrease clockwise or anticlockwise [24,35]. We detect no such intensity progression in the CDW peak intensities in our studies of the NC-CDW state of $1T$-TaS_2. Rather, in our FFTs we find a clockwise rotation of two intense satellite peaks around the central CDW peaks, connected to the domain formation and chiral CDW lattice distortions from the average CDW lattice. Figure 4(d) shows arrows pointing from CDW_{ave} maxima to the nearest imaged atom evincing a very similar chiral pattern to Fig. 4(a). In each, shifts are in the counterclockwise direction leading to clear domain formation. In short, Fig. 4(d) shows the CDW displacements in the limit of a perfectly incommensurate CDW lattice which has very strong homogenous coupling to the atomic lattice with no energy cost for CDW deformations. This strongly suggests that the chiral domains formed in the NC-CDW state of $1T$-TaS_2 are driven through a strong coupling of the CDW state to the atomic lattice, not through orbital ordering which is believed to drive chiral CDW orders in related TMDs. We can understand the origin of the strong coupling of the CDW to the lattice in the NC-CDW state of $1T$-TaS_2 in the following way. Within a star of David, there are 13 $5d$ electrons, one from each Ta ion, 12 of which are bonded leaving a single extra electron per star [39]. The strong coupling of the CDW state to the lattice likely originates from the Coulomb interaction of these extra electrons with the Ta lattice; these extra electrons preferentially locate near Ta ions.

Previous chiral CDW orders found in the TMDs have been attributed to orbital ordering. In the NC-CDW state of the TMD $1T$-TaS_2, we find instead a CDW state with chiral domains which appears to originate from a strong coupling of an incommensurate CDW to the lattice. Further, our work suggests a competition between lattice coupling, producing the chiral domains within the NC-CDW state, and the energy gained from the electronic structure, in which a particular Q vector is favored, leading to the commensurate C-CDW state at low temperatures. A natural way to theoretically model and explore this interplay would be to explicitly include CDW-lattice coupling in existing McMillian-type Landau free-energy frameworks [3,40–42]. Such domain chirality may be a more general phenomenon which can be explored in systems hosting incommensurate CDW states, including in TMDs.

Methods. STM measurements were conducted at room temperature and ultrahigh vacuum ($\sim 10^{-9}$ Torr) using an RHK PanScan STM. The chemically etched tungsten tip was annealed and then sharpened using electron bombardment *in situ*. High-quality single crystals of $1T$-TaS_2 studied in this Letter were purchased from HQ Graphene. Samples were cleaved in UHV.

This work was supported by the National Science Foundation under Grant No. DMR-1904918.

[1] D. Kühn, M. Muller, F. Sorgenfrei, E. Giangrisostomi, R. M. Jay, R. Ovsyannikov, N. Martensson, D. Sanchez-Portal, and A. Fohlisch, Directional sub-femtosecond charge transfer dynamics and the dimensionality of $1T$-TaS_2, Sci. Rep. **9**, 488 (2019).

[2] T. Ritschel, H. Berger, and J. Geck, Stacking-driven gap formation in layered $1T$-TaS_2, Phys. Rev. B **98**, 195134 (2018).

[3] K. Nakanishi, H. Takatera, Y. Yamada, and H. Shiba, The nearly commensurate phase and effect of harmonics on the successive phase transition in $1T$-TaS_2, J. Phys. Soc. Jpn. **43**, 1509 (1977).

[4] S. Tanda, T. Sambongi, T. Tani, and S. Tanaka, X-ray study of charge density wave structure in $1T$-TaS_2, J. Phys. Soc. Jpn. **53**, 476 (1984).

[5] R. E. Thomson, B. Burk, A. Zettl, and J. Clarke, Scanning tunneling microscopy of the charge-density-wave structure in $1T$-TaS_2, Phys. Rev. B **49**, 16899 (1994).

[6] K. T. Law and P. A. Lee, $1T$-TaS_2 as a quantum spin liquid, Proc. Natl. Acad. Sci. USA **114**, 6996 (2017).

[7] D. Cho, S. Cheon, K.-S. Kim, S.-H. Lee, Y.-H. Cho, S.-W. Cheong, and H. W. Yeom, Nanoscale manipulation of the Mott insulating state coupled to charge order in $1T$-TaS_2, Nat. Commun. **7**, 10453 (2016).

[8] L. Ma, C. Ye, Y. Yu, X. F. Lu, X. Niu, S. Kim, D. Feng, D. Tománek, Y.-W. Son, X. H. Chen, and Y. Zhang, A metallic mosaic phase and the origin of Mott-insulating state in $1T$-TaS_2, Nat. Commun. **7**, 10956 (2016).

[9] L. Perfetti, P. A. Loukakos, M. Lisowski, U. Bovensiepen, H. Berger, S. Biermann, P. S. Cornaglia, A. Georges, and M. Wolf, Time Evolution of the Electronic Structure of $1T$-TaS_2 through the Insulator-Metal Transition, Phys. Rev. Lett. **97**, 067402 (2006).

[10] C. J. Butler, M. Yoshida, T. Hanaguri, and Y. Iwasa, Mottness versus unit-cell doubling as the driver of the insulating state in $1T$-TaS_2, Nat. Commun. **11**, 2477 (2020).

[11] T.-R. T. Han, F. Zhou, C. D. Malliakas, P. M. Duxbury, S. D. Mahanti, M. G. Kanatzidis, and C.-Y. Ruan, Exploration of metastability and hidden phases in correlated electron crystals visualized by femtosecond optical doping and electron crystallography, Sci. Adv. **1**, e1400173 (2015).

[12] Y. Liu, R. Ang, W. J. Lu, W. H. Song, L. J. Li, and Y. P. Sun, Superconductivity induced by Se-doping in layered charge-density-wave system $1T$-$TaS_{2-x}Se_x$, Appl. Phys. Lett. **102**, 192602 (2013).

[13] L. J. Li, W. J. Lu, X. D. Zhu, L. S. Ling, Z. Qu, and Y. P. Sun, Fe-doping-induced superconductivity in the charge-density-wave system $1T$-TaS_2, Europhys. Lett. **97**, 67005 (2012).

[14] S. Qiao, X. Li, N. Wang, W. Ruan, C. Ye, P. Cai, Z. Hao, H. Yao, X. Chen, J. Wu, Y. Wang, and Z. Liu, Mottness Collapse in $1T$-$TaS_{2-x}Se_x$ Transition-Metal Dichalcogenide: An Interplay Between Localized and Itinerant Orbitals, Phys. Rev. X **7**, 041054 (2017).

[15] L. Stojchevska, I. Vaskivskyi, T. Mertelj, P. Kusar, D. Svetin, S. Brazovskii, and D. Mihailovic, Ultrafast switching to a stable hidden quantum state in an electronic crystal, Science **344**, 177 (2014).

[16] I. Vaskivskyi, J. Gospodaric, S. Brazovskii, D. Svetin, P. Sutar, E. Goreshnik, I. A. Mihailovic, T. Mertelj, and D. Mihailovic, Controlling the metal-to-insulator relaxation of the metastable hidden quantum state in $1T$-TaS_2, Sci. Adv. **1**, e1500168 (2015).

[17] Y. A. Gerasimenko, P. Karpov, I. Vaskivskyi, S. Brazovskii, and D. Mihailovic, Intertwined chiral charge orders and topological stabilization of the light-induced state of a prototypical transition metal dichalcogenide, npj Quantum Mater. **4**, 32 (2019).

[18] K. Bu, W. Zhang, Y. Fei, Z. Wu, Y. Zheng, J. Gao, X. Luo, Y.-P. Sun, and Y. Yin, Possible strain induced Mott gap collapse in $1T$-TaS_2, Commun. Phys. **2**, 146 (2019).

[19] T. Ritschel, J. Trinckauf, G. Garbarino, M. Hanfland, M. v. Zimmermann, H. Berger, B. Buchner, and J. Geck, Pressure dependence of the charge density wave in $1T$-TaS_2 and its relation to superconductivity, Phys. Rev. B **87**, 125135 (2013).

[20] B. Sipos, A. F. Kusmartseva, A. Akrap, H. Berger, L. Forró, and E. Tutis, From Mott state to superconductivity in $1T$-TaS_2, Nat. Mater. **7**, 960 (2008).

[21] M. Yoshida, Y. Zhang, J. Ye, R. Suzuki, Y. Imai, S. Kimura, A. Fujiwara, and Y. Iwasa, Controlling charge-density-wave states in nano-thick crystals of $1T$-TaS_2, Sci. Rep. **4**, 7302 (2014).

[22] M. Yoshida, R. Suzuki, Y. Zhang, M. Nakano, and Y. Iwasa, Memristive phase switching in two-dimensional $1T$-TaS_2 crystals, Sci. Adv. **1**, e1500606 (2015).

[23] M. R. Norman, The challenge of unconventional superconductivity, Science **332**, 196 (2011).

[24] J. J. Gao, W. H. Zhang, J. G. Si, X. Luo, J. Yan, Z. Z. Jiang, W. Wang, H. Y. Lv, P. Tong, W. H. Song, X. B. Zhu, W. J. Lu, Y. Yin, and Y. P. Sun, Chiral charge density waves induced by Ti-doping in $1T$-TaS_2, Appl. Phys. Lett. **118**, 213105 (2021).

[25] X. Song, L. Liu, Y. Chen, H. Yang, Z. Huang, B. Hou, Y. Hou, X. Han, H. Yang, Q. Zhang, T. Zhang, J. Zhou, Y. Huang, Y. Zhang, H.-J. Gao, and Y. Wang, Atomic-scale visualization of chiral charge density wave superlattices and their reversible switching, Nat. Commun. **13**, 1843 (2022).

[26] T. Ishiguro and H. Sato, Electron microscopy of phase transformations in $1T$-TaS_2, Phys. Rev. B **44**, 2046 (1991).

[27] K. Momma and F. Izumi, Vesta.3 for three-dimensional visualization of crystal, volumetric and morphology data, J. Appl. Crystallogr. **44**, 1272 (2011).

[28] See Supplemental Material at http://link.aps.org/supplemental/10.1103/PhysRevB.106.L081407 for a topographic image of a single domain, for details on simulating the NC-CDW $1T$-TaS_2 topography, for figures showing arrows drawn from CDW_{ave} to nearest Ta ions, for further discussion on extracting the displacement field, for an analysis of the simulated topography

evincing the same intradomain chiral nature of the NC-CDW state found from the data, and for additional details on the link between satellite peaks and domain chirality.

[29] C. B. Scruby, P. M. Williams, and G. S. Parry, The role of charge density waves in structural transformations of $1T$-TaS_2, Philos. Mag. **31**, 255 (1975).

[30] D. F. Shao, R. C. Xiao, W. J. Lu, H. Y. Lv, J. Y. Li, X. B. Zhu, and Y. P. Sun, Manipulating charge density waves in $1T$-TaS_2 by charge-carrier doping: A first-principles investigation, Phys. Rev. B **94**, 125126 (2016).

[31] W. Wang, D. Dietzel, and A. Schirmeisen, Lattice discontinuities of $1T$-TaS_2 across first order charge density wave phase transitions, Sci. Rep. **9**, 7066 (2019).

[32] A. W. Tsen, R. Hovden, D. Wang, Y. D. Kim, J. Okamoto, K. A. Spoth, Y. Liu, W. Lu, Y. Sun, J. C. Hone, L. F. Kourkoutis, P. Kim, and A. N. Pasupathy, Structure and control of charge density waves in two-dimensional $1T$-TaS_2, Proc. Natl. Acad. Sci. USA **112**, 15054 (2015).

[33] M. Lawler, K. Fujita, J. Lee, A. Schmidt, Y. Kohsaka, C. K. Kim, H. Eisaki, S. Uchida, J. Davis, J. Sethna *et al.*, Intra-unit-cell electronic nematicity of the high-T_c copper-oxide pseudogap states, Nature (London) **466**, 347 (2010).

[34] S. Gao, F. Flicker, R. Sankar, H. Zhao, Z. Ren, B. Rachmilowitz, S. Balachandar, F. Chou, K. S. Burch, Z. Wang, J. van Wezel, and I. Zeljkovic, Atomic-scale strain manipulation of a charge density wave, Proc. Natl. Acad. Sci. USA **115**, 6986 (2018).

[35] J. Ishioka, Y. H. Liu, K. Shimatake, T. Kurosawa, K. Ichimura, Y. Toda, M. Oda, and S. Tanda, Chiral Charge-Density Waves, Phys. Rev. Lett. **105**, 176401 (2010).

[36] A. Kłosiński, A. M. Oleś, C. Efthimia Agrapidis, J. van Wezel, and K. Wohlfeld, Chalcogenic orbital density waves in the weak- and strong-coupling limit, Phys. Rev. B **103**, 235123 (2021).

[37] J. van Wezel, Chirality and orbital order in charge density waves, Europhys. Lett. **96**, 67011 (2011).

[38] Y. Peng, X. Guo, Q. Xiao, Q. Li, J. Strempfer, Y. Choi, D. Yan, H. Luo, Y. Huang, S. Jia, O. Janson, P. Abbamonte, M. van den Brink, and J. van Wezel, Observation of orbital order in the van der Waals material $1T$-$TiSe_2$, Phys. Rev. Research **4**, 033053 (2022).

[39] M. Kratochvilova, A. D. Hillier, A. R. Wildes, L. Wang, S.-W. Cheong, and J.-G. Park, The low-temperature highly correlated quantum phase in the charge-density-wave $1T$-TaS_2 compound, npj Quantum Mater. **2**, 42 (2017).

[40] W. L. McMillan, Landau theory of charge-density waves in transition-metal dichalcogenides, Phys. Rev. B **12**, 1187 (1975).

[41] W. L. McMillan, Theory of discommensurations and the commensurate-incommensurate charge-density-wave phase transition, Phys. Rev. B **14**, 1496 (1976).

[42] K. Nakanishi and H. Shiba, Domain-like incommensurate charge-density-wave states and the first-order incommensurate-commensurate transitions in layered tantalum dichalcogenides. I. $1T$-polytype, J. Phys. Soc. Jpn. **43**, 1839 (1977).